AIAA JOURNAL
Vol. 40, No. 5, May 2002

# Numerical Simulation of Adaptive Control: Application to Unstable Solid Rocket Motors

M. Mettenleiter*
*Ecole Centrale Paris, F-92295 Châtenay-Malabry Cedex, France*
F. Vuillot†
*ONERA, Châtillon, F-92322 Châtillon Cedex, France*
and
S. Candel‡
*Ecole Centrale Paris, F-92295 Châtenay-Malabry Cedex, France*

**Current developments in the numerical simulation of active control are described. The objective of this investigation is to devise software tools for the development of active control. The present approach uses a numerical simulation of the system based on the Navier–Stokes equations. It differs from the more standard simulations relying on lower-order dynamic models. The main difficulties associated with the present strategy are related to the representation of the actuator in the flow simulation module and with the interfacing of this module with the adaptive control routine. These issues require careful treatment to obtain a suitable numerical model of flow control. It is first shown that the actuator may be described by a distribution of sources in the field. The time steppings needed by the flow simulation module and by the control unit differ widely. (The ratio between the time steps is of the order of 100 or more.) This constitutes a source of perturbation, and it may introduce unwanted high-frequency components in the flow simulation. It is shown that this problem is alleviated by placing numerical filters at the controller input and output. A set of calculations are carried out to simulate vortex shedding instabilities of a simplified solid propellant rocket. These instabilities are then adaptively controlled. This example serves to illustrate the simulation methodology and provides insights into the operation of the flow controller.**

## Introduction

ACTIVE control strategies have mainly been developed from experiments. More recent efforts have been directed at the computer simulation of control to test and improve control algorithms. Numerical simulations complement experiments, and they have had considerable impact on the development of active flow control. The present investigation aims to devise reliable tools for the numerical simulation of active control. It addresses problems arising when attempting to couple a flow simulation module and an adaptive control algorithm. The study is motivated by research into the control of vortex driven instabilities found in segmented solid rocket motors. Such motors are known to develop low-amplitude pressure and thrust oscillations at frequencies of the first longitudinal acoustic modes (for example, see Refs. 1–3). The oscillation is at low frequency, and it may couple with the launcher's structural modes. The driving mechanisms are linked to internal flow instability. The strong coupling with acoustics generates large-scale coherent vortices.

This process is simulated in the present work by solving the Navier–Stokes equations using the Sierra software. The flow simulation module has been used extensively to analyze vortex instabilities in configurations of interest to solid propellant propulsion. It is used here as a platform for active control. Numerical simulation is now increasingly used to predict the behavior of unstable subscale solid rocket motors. A recent example by Le Breton et al.[4] shows industrial applications of this type of simulation.

After a short review of the literature dealing with simulation of flow control, the flow solver module is briefly described. One important aspect of the problem is to devise a suitable representation of an actuator or of a set of actuators. It is shown that this is best accomplished by distributing sources in the field. This representation is also closer to the possible use of a controlled injection of an evaporating and/or reacting substance in an actual motor. Such a physical device would provide a distributed source of mass and a source or sink of energy. Momentum exchange might also take place depending on the type of injection geometry.

Modifications of the Sierra code[2,5] are described and a series of open-loop tests are carried out to show that the sources operate as expected. Problems related to the coupling of the flow simulation module with the control algorithm are considered. Specific issues arise because flow simulation and control require very different time sampling rates. The time step of the flow solver is much smaller than the sampling period of the controller. It is then necessary to take some precautions when dealing with the input and output of the control routine. The last section provides numerical simulations of vortex instabilities in a small rocket motor and control of these instabilities using an adaptive algorithm. In the first situation, the controller input is a pressure signal provided by a sensor located near the nozzle, whereas the actuator is located near the motor head. In the second case, the sensor is assumed to be sensitive to vorticity, and the actuator is located near the point where vortices are being shed. These two examples serve to show that the active control simulator is flexible and may be used to study the control strategy and examine the modification of the flow under control.

## Active Control Simulation Studies

The simulation of active control of instabilities and noise may be divided in two main groups. The first group consists of studies based on simplified dynamic models coupled to simple or more complex control schemes. A typical example from the field of sound and vibration control is given by Koshigoe et al.[6] This paper considers adaptive algorithms to reduce the noise from a confined cavity. Vibrations originating from outside the cavity walls may induce large

Received 27 March 2000; revision received 20 April 2001; accepted for publication 12 November 2001. Copyright © 2002 by the American Institute of Aeronautics and Astronautics, Inc. All rights reserved. Copies of this paper may be made for personal or internal use, on condition that the copier pay the $10.00 per-copy fee to the Copyright Clearance Center, Inc., 222 Rosewood Drive, Danvers, MA 01923; include the code 0001-1452/02 $10.00 in correspondence with the CCC.

*Research Scientist, Laboratoire EM2C, Centre National de la Recherche Scientifique; currently Research Engineer, Ingenieurburo für Thermoakustik, GmbH, D-82194 Grobenzell, Germany.
†Research Scientist. Member AIAA.
‡Professor of Aerospace Engineering, Laboratoire EM2C, Centre National de la Recherche Scientifique; also Professor, Institut Universitaire de France. Senior Member AIAA.

pressure fluctuations in the cavity. The problem arises during space launcher takeoff. The noise induced under the fairings may harm the payload and have detrimental effects on the future operation of the spacecraft. A dynamic model of the system is formulated and used to test the filtered X-least-mean-square (X-LMS) algorithm with off-line identification of the secondary path.[7] Online identification is explored with the same model in a more recent study,[8] and the LMS algorithm is compared to other control schemes[9] with regard to the convergence rate.

In the field of combustion instability, Hathout et al.[10] develop a dynamic first-order model of thermoacoustic interactions in a small laminar burner. This model is then used to design a controller and simulate its operation. The control algorithm is then used in the experiment. To account for changes in the system dynamics, an adaptive controller is devised and compared with simulations carried out with an LMS algorithm.[11] Culick et al.[12] consider linear and nonlinear coupling in their comprehensive dynamic model of instability. It is, thus, possible to describe some of the effects that lead to limit cycle oscillations found in practical systems. Yang and Fung[13] use this general formalism to design a proportional–integral controller of pressure oscillations in a combustion chamber. Annaswamy et al.[14] study the influence of mode coupling on controller design using the same general formulation. Koshigoe et al.[15] propose an adaptive algorithm with online identification to control a dynamic model of combustion instability.

In the second group of studies dealing with active control simulation, the flow is calculated by solving the Navier–Stokes equations. This provides a more realistic description of the flow dynamics and of the complex couplings taking place in practical devices. This approach uses the recent advances made in computational fluid dynamics. Menon[16] is perhaps the first to investigate active control in an unsteady simulation of a dump combustor typifying the geometry of a two-dimensional ramjet. The feedback loop comprises a simple gain and phase shift applied to a pressure sensor signal and reinjected through a loudspeaker located at the backward facing step. Neumeier and Zinn[17] devise a special state observer that identifies the unstable modes of the system. The modes are then amplified and phase delayed by a controller and reinjected into the computational domain. The balance equations are solved in one dimension. Kestens[18] considers the adaptive (LMS) multiple channel control of aeroacoustic instabilities of cavities driven by an adjacent flow. The Navier–Stokes equations are solved in two dimensions. An actuator represented by a vibrating boundary or by a pulsed jet is used to reduce the pressure level observed by different sensors.

Analysis of work belonging to this second group shows some success, but indicates that the methodology needs further consolidation. It is our aim to devise a complete simulation of active control by coupling a nonsteady Navier–Stokes solver with an adaptive controller. The analysis will be carried out using an adaptive scheme for the following reasons: 1) The system to be controlled is nonlinear and may change with time. 2) Control using adaptive methods has been successfully demonstrated in related experiments. 3) The controller has a self-adjusting capability. No attempt was made to test a simpler linear (nonadaptive) controller.

The following aspects are considered in the next sections: 1) numerical representation of the actuator, 2) actuator effect in open-loop simulation tests, and 3) problems of controller interfacing.

## Flow Simulation in the C1-Geometry

The Sierra code is used to simulate the large scales of flow to analyze aeroacoustic instabilities generated in internal geometries found in solid rocket motors. The code operates in the planar or axisymmetric modes. It was designed by Lupoglazoff and Vuillot.[5] (See Ref. 5 and references included for details.) The Navier–Stokes equations are solved with a second-order finite volume centered scheme. Time marching is explicit and the MacCormack predictor/corrector method is used. Artificial viscosity is calculated with the Jameson method (see Ref. 19). Sierra is used in what follows to simulate the flow in a specific geometry designated as C1. This is the first test case of a systematic research program on the aerodynamics of segmented solid rocket motors. This computational case was defined by ONERA to study the strong aeroacoustic oscillations resulting from vortex shedding from the propellant edge coupled with one of the modes of the system.[20] This generic case is well documented and requires a limited amount of grid nodes (around 10,000), allowing long computational sequences.

### Numerical Accuracy and Simulation Parameters

Accuracy is a central question in the present investigation. Calculations should provide a physically correct description of the unsteady flow in the system. It is first important to check that the solution does not depend on the grid. The actuator representation and the coupling requirements between the flow solver and the controller also constitute critical aspects. Systematic tests have been carried out to check that the actuator description is suitable. (One test is included later.) Conditions assuring that the coupling does not induce spurious perturbations are discussed in the next section.

Grid independence of the solution was checked by replacing the standard mesh of $318 \times 31$ nodes by a finer grid of $454 \times 43$ points. The C1 geometry features a marked acoustic resonance that structures the large scales of the flow. Vortices are shed in the present case from the edge of the block of propellant. The flow in this region is essentially governed by a balance between inertial and pressure forces, which is typical of such solid propellant flows. Under such circumstances, turbulence is of lesser importance, and it is not necessary to use a subgrid model. It was also shown by Comte et al.[21] that a full three-dimensional large eddy simulation, including a subgrid scale model, did not change the overall structure of the unsteady flow. In practice, numerical viscosity acts as a subgrid model and dissipates the smaller scales of turbulence.

In the present simulations, the flow is nonreactive but allows a suitable description of the vortex-acoustic resonance in such a flow geometry. Parameters adopted in the simulations are gathered in Table 1. Indices $i$ and $j$ specify locations of actuators and sensors with respect to the mesh. Figure 1 shows their positions in the computational domain. Pressure sensors are placed at the head end, $p_H$, and at the nozzle entrance, $p_A$. An additional sensor is placed just upstream of $p_A$ to measure the local pressure difference ($\Delta p = p_A - p_B$). In the detection of $\Delta p$, the aim is to filter out the

**Table 1 Parameters of the C1 computations**

| Parameter | Case 1 | Case 2 |
|---|---|---|
| Number of grid points | $318 \times 31$ | $318 \times 31$ |
| Pressure sensor $p_B$ $(i, j)$ | (210, 1) | (210, 1) |
| Pressure sensor (error signal) $p_A$ $(i, j)$ | (245, 1) | —— |
| Forward plane pressure sensor $p_H$ $(i, j)$ | (1, 30) | (1, 30) |
| $x$-velocity sensor $u_E$ $(i, j)$ | (245, 24) | (245, 24) |
| Vorticity sensor (error signal) $\omega_E$ $(i, j)$ | —— | (245, 24) |
| Actuator position $(i_d, i_f, h)$ | (1, 2, 30) | (64, 74, 5) |
| Reference length, m | 0.47 | 0.47 |
| Reference velocity, $ms^{-1}$ | 1075.3 | 1075.3 |
| Integration time step $\Delta t$, $\mu s$ | 0.244 | 0.244 |
| Resonance frequency (close to 2L ), Hz | 2540 | 2540 |

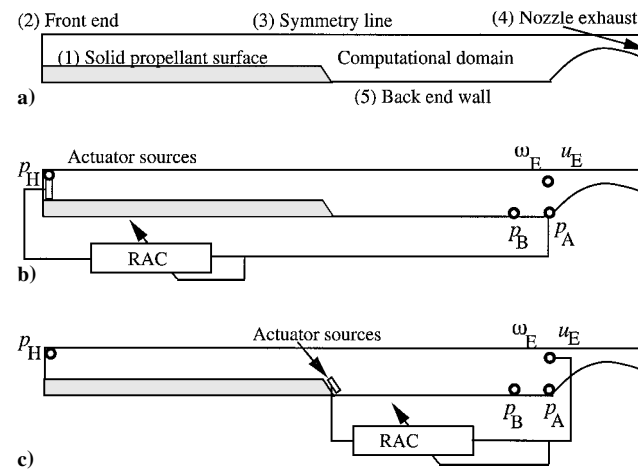


**Fig. 1 C1 geometry: a) definition of computational domain, b) locations of actuator sources and sensors for case 1, and c) locations of actuator sources and sensors for case 2.**

acoustic pressure signal. The pressure difference is then proportional to the hydrodynamic pressure gradient. The filtering is based on the difference in characteristic length scales between acoustic and hydrodynamic perturbations. Two additional sensors placed at the nozzle entrance detect axial velocity and vorticity fluctuations $u_E$ and $\omega_E$.

The computational domain is represented in Fig. 1. The lower boundary 1 delivers a uniform stream of gases and represents the solid propellant surface. The mass flow rate per unit surface is imposed at this boundary; the gas temperature is prescribed, and the tangential velocity component is zero at this limit. Boundary 2 represents the motor front head; the velocity vanishes on this boundary, and the temperature is imposed. Line 3 is a symmetry plane. The outflow in section 4 is supersonic, so that numerical boundary conditions in this section are treated by simple extrapolation from the computational domain. At wall 5 the flow velocity vanishes, and the temperature is imposed.

**Actuator Representation**

The actuators will be defined as distribution of sources on the computational mesh. As explained earlier, these sources correspond to mass, momentum, and energy addition. The actuator location is specified by the first and last values ($i_d$ and $i_f$) of index $i$, corresponding to the source, and by the transverse size of the source specified in terms of elementary cells by index $h$ (Table 1). The actuator source locations are shown in Fig. 1.

In a first attempt at controlling the instabilities observed in the C1 case, the actuator was simulated by a modified front-end boundary condition. Perturbations were imposed on the incoming characteristic lines, whereas outgoing waves were allowed to propagate out of the domain without reflection. Systematic tests carried out in this situation indicated that the simulated flowfield did not respond adequately to the imposed fluctuations. For a given modulation frequency differing from that of the instability and for a small level of perturbation, one expected to find a superposition of acoustic waves in the system and a beating between these two waves if the frequencies are close. If this were the case, it would have been possible to act on the signal delivered by the pressure sensor to control the vortex shedding. Calculations, however, indicated that beating was only produced at the beginning of the simulation and that vortices were very rapidly synchronized to the excitation signal introduced by the actuator. Closed-loop control could not be achieved under these circumstances. This behavior was due to the modified boundary condition used to represent the actuator. Because the boundary did not reflect the incident waves, the resonant properties of the system were changed, and the vortex shedding phenomenon was altered.

It was then decided to use an alternative method to model the actuator. The boundary conditions were left untouched, but source terms were distributed in the field. A somewhat similar approach was devised independently by Mohanraj et al.,[22] who use sources in a one-dimensional version of Euler's equations.

Without describing the details of the Sierra code, we only summarize the steps required to incorporate source terms in the balance equations.

1) In the first step, one has to specify the number, location, and type of source. This is done in a driver module that is read at the simulation beginning. This driver also contains information on the sensors used in the control scheme.

2) During the calculation and at each time step, the sources and sensors are updated.

3) After each step the sources are added to the right-hand side of the discretized balance equations.

If $\dot{\omega}_s$ designates the volumetric rate of mass addition, the discretized balance of mass, momentum, and energy are modified as follows:

$$\rho_c^{n+1} = \rho^{n+1} + \delta t \dot{\omega}_s^n \tag{1}$$

$$(\rho u)_c^{n+1} = (\rho u)^{n+1} + \left(\delta t \dot{\omega}_s^n\right) u_s^n \tag{2}$$

$$(\rho v)_c^{n+1} = (\rho v)^{n+1} + \left(\delta t \dot{\omega}_s^n\right) v_s^n \tag{3}$$

$$(\rho E)_c^{n+1} = (\rho E)^{n+1} + \left(\delta t \dot{\omega}_s^n\right)(e_s + k_s)^n \tag{4}$$

The superscript $n$ corresponds to time discretization and subscript $c$ designates the controlled variables. Velocity components $u_s$ and $v_s$ and the internal energy of the injected stream $e_s$ may be freely specified. The kinetic energy $k_s$ is a function of $u_s$ and $v_s$. In the present calculations, the value adopted for the internal energy $e_s$ is that of the surrounding fluid. To focus on mass addition effects, the velocities $u_s$ and $v_s$ and the corresponding kinetic energy $k_s$ are set equal to zero. The rate of mass addition $\dot{\omega}_s$ may be defined in various ways. In open-loop tests, this term is explicitely defined by one of the following expressions:

$$\dot{\omega}_s = a \tag{5}$$

$$\dot{\omega}_s = b \sin[2\pi f(t - t_0) + \phi] \tag{6}$$

$$\dot{\omega}_s = cS(t, t_1, t_2; f_1, f_2) \tag{7}$$

where $a$, $b$, and $c$ are constants, $f$ is a given frequency, $t_0$ is a time origin, and the function $S$ defines a sinewave with a frequency sweep from $f_1$ to $f_2$ begining at time $t_1$ and ending at $t_2$. It is, thus, possible to simulate a constant injection of mass ($a \neq 0$), a sinusoidal modulation ($b \neq 0$), or a linear frequency modulated sinusoide ($c \neq 0$). The mass injection term $\dot{\omega}_s$ may also follow the controller output, which is designated in what follows as active control routine (RAC): $\dot{\omega}_s = \mathrm{RAC}(t)$.

In this application, the adaptive controller RAC is fed by one of the sensors defined in Fig. 1. Tests of the source terms were carried out systematically to verify the proper operation of the concept. A constant section duct with closed/open left and right sections is filled with fluid. The mass flowing out of the tube exactly equals that injected by the sources. In a second test, a source was placed at various sections of the duct to excite the acoustic modes of the system. The mesh in this case comprised $61 \times 20$ nodes, and the excitation frequency is that of the three-quarter wave mode corresponding to the second eigenmode of a closed–open channel. The source was distributed over the height of the duct and occupied two cells in the axial direction. In the case shown in Fig. 2, the source is located in the first two cells, which correspond to a pressure antinode. The acoustic mode develops uniformly in the transverse direction, and the pressure and velocity distributions coincide with those expected theoretically. Other test cases show that the source terms incorporated in the Sierra code allow simulations of acoustic modulation without modification of the boundary conditions.

A second test series aims to analyze the response of the vortex driven flow in the C1 configuration under an external excitation. Parameters are those of case 1 in Table 1. The calculation begins with an established oscillation in the flow. Effects of different levels of source excitation are displayed in Fig. 3. The signal detected by the pressure sensor $p_A$ is shown in Fig. 3a. This signal will serve later as an error signal in the control scheme of the first simulation. The signal detected by the differential pressure signal $\Delta p$ is shown in Fig. 3b. Both signals feature the instability frequency. When the excitation amplitude is augmented, two frequencies are detected; a further increase in amplitude leads to a decrease of the instability frequency level. Analysis of other sensor signals confirm this behavior. (For more detailed information, see Ref. 23.)

The preceding calculations indicate that the C1 configuration responds to the new source terms placed in the field. The following points are noticeable:

1) The instability phenomenon coexists with the frequency delivered by the actuator when the level of excitation is low.

2) The frequency shifts toward the excitation frequency when the level of modulation is larger.

3) The vortex shedding process is reorganized when the excitation frequency is very large.

Before describing closed-loop calculations, we now consider the control algorithm and examine issues related to interfacing.

## Interfacing the Control Algorithm with the Flow Simulation Module

The interface between the flow simulation module Sierra and the subroutine RAC, which corresponds to the adaptive controller, is designed to come as close as possible to a typical experimental configuration. The Sierra code is then used as a black box, providing signals

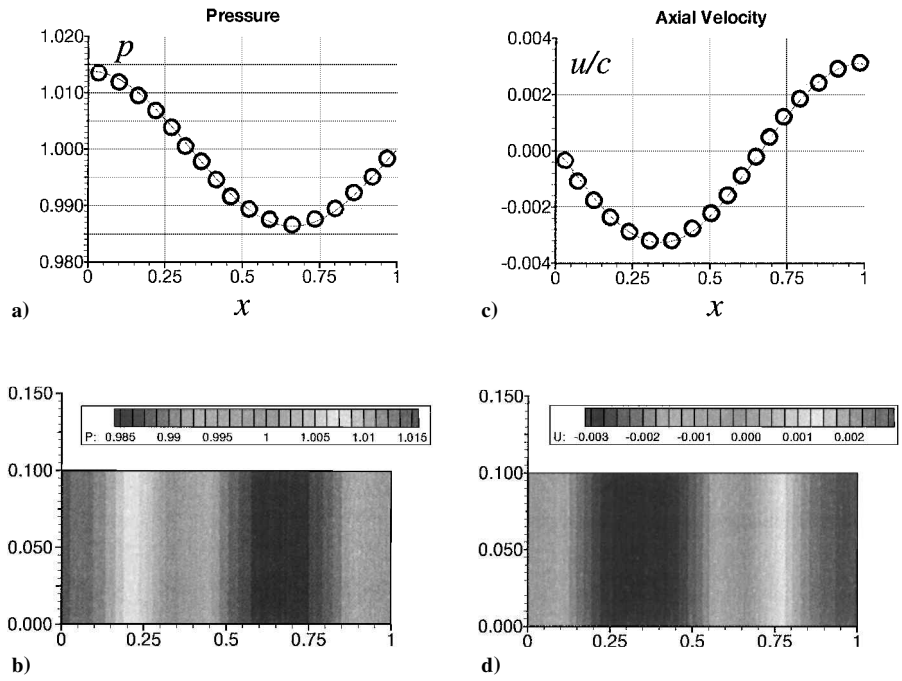


**Fig. 2 Excitation at a pressure antinode: a) spatial distribution of pressure (bars), b) spatial distribution of acoustic velocity (velocity amplitude divided by the speed of sound), c) signals plotted as a function of the axial coordinate, and d) pressure and velocity fields plotted on a scale of gray levels.**

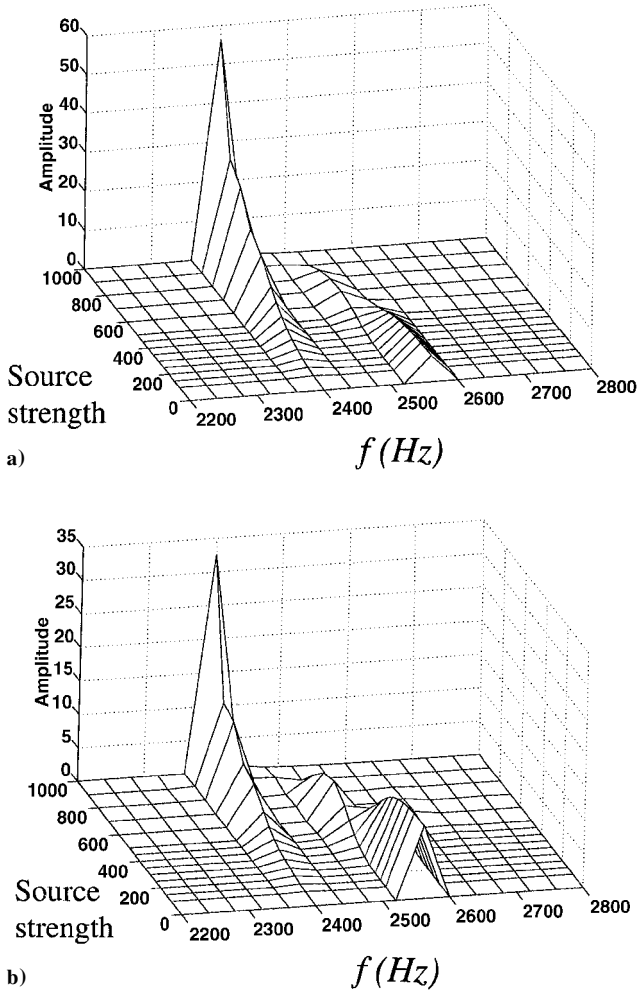


**Fig. 3 Influence of a single control source on pressure signal detected by a) the $p_A$ error sensor and b) the differential pressure sensor $p_A - p_B$; the level of excitation varies from low to high.**

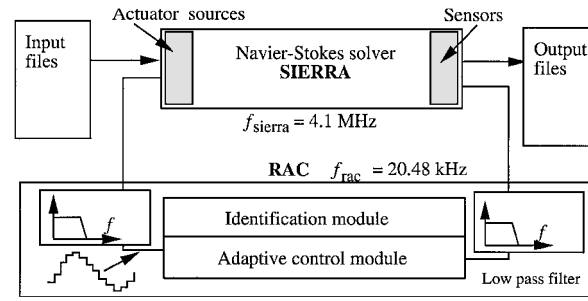


**Fig. 4 Block diagram of the Sierra interface with the adaptive controller RAC.**

detected by different sensors and receiving the signal driving the actuator. The integration step in the simulations is of $\Delta t = 2.44\,10^{-7}$ s, which corresponds to a sampling frequency $f_{\text{sierra}} = 4.096 \times 10^6$ Hz. Results are recorded periodically every $d_w = 25\Delta t$. (The writing frequency is $f_w = 1.64 \times 10^5$ Hz.) It is not necessary and not recommended to use the adaptive filter at these very high rates. Such frequencies would require very long filters (with more than a few hundred coefficients) to represent the system with sufficient precision. The filter renewal should be effected at a much lower rate, typically at a frequency $f_{\text{rac}} = 20{,}480$ Hz. This value corresponds to the Sierra frequency divided by a factor $d_s = 200$.

To link a typical flow experiment featuring an analog sensor to the discrete control algorithm one uses an antialiasing filter (AAF). The same precaution seems necessary in connecting the flow simulation module Sierra to the control routine RAC. The sampling rate reduction by a large factor $d_s = 200$ induces a loss of information and may lead to problems of spectral overlap similar to those found when analog signals are sampled into discrete sequences. This justifies filtering of the controller input with an AAF as shown in Fig. 4. The flow simulation module Sierra yields an input to the controller RAC at each integration step. One may then choose to keep each $d_s$ value provided by Sierra, or one may first low-pass filter the values generated by Sierra and then keep the result every $d_s$ sample.

A similar situation prevails at the controller output. One possibility is to use a sample and hold, which keeps a constant value of

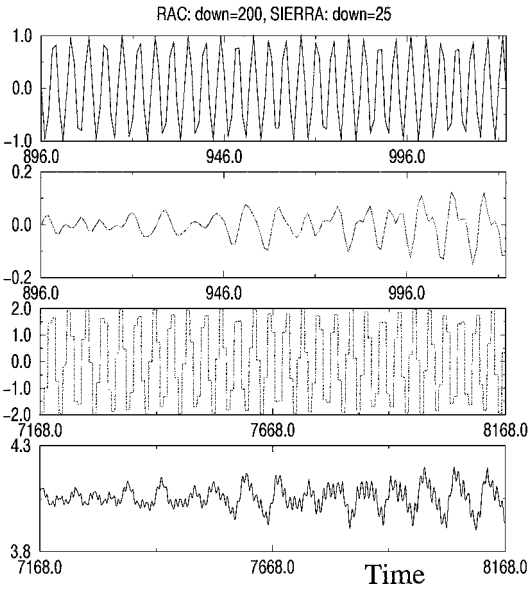


**a) No filtering**

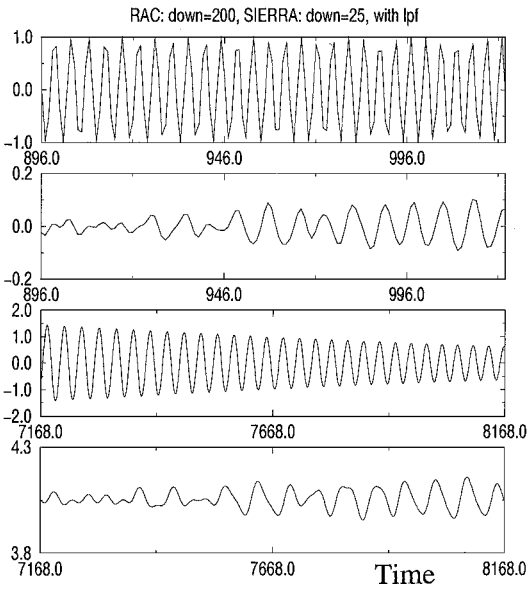


**b) With filtering**

**Fig. 5 Comparison between actuator and sensor signal records. From top to bottom: actuator signal output generated by RAC, pressure signal input to RAC, actuator signal input to Sierra, and pressure signal output from Sierra, $d_w = 25$ and $d_s = 200$.**

the RAC output during the following $d_s$ integration steps of Sierra. Alternatively, one may low-pass filter the output to eliminate the high frequencies introduced by the successive jumps in the sampled and blocked values returned by the controller (see Fig. 4).

The effects of filtering may be examined with the following tests. In a first trivial case (which is not shown here), $d_w = d_s = 25$. This means that the sensor values are written at the same frequency by Sierra as they are updated and written by RAC. Hence, the sensor and actuator signals measured by RAC and Sierra are identical. In the second test case, the sampling rates differ: $d_w = 25$ and $d_s = 200$. These values are adopted later on in the control simulations. The corresponding results are displayed in Fig. 5. (The upper plot is the actuator signal generated by RAC, the second plot is the pressure sensor measured by RAC, the third plot is the actuator signal measured by Sierra, and the bottom plot is the pressure sensor measured by Sierra.) The actuator signal measured by Sierra clearly shows the discretization effect. In this case, Sierra receives a discretized sinusoid (third curve from the top). Note that this is not a quantization error, but is the consequence of the sample and hold operation of the controller output. Although this would have no effect on the controller performance, it generates high-frequency components as seen in the signal detected by the pressure sensor, which features high-frequency oscillations (lower plot in Fig. 5a). These oscillations were not observed in the preceding test. The high frequencies introduced by the sampled signal feeding the actuator interfere with the calculation. When the controller input is formed by the samples without filtering (second plot from the top), high-frequency components are present. This perturbs the controller and the initial frequency is less visible.

Using the same downsampling as in the preceding test ($d_w = 25$ and $d_s = 200$), but including a low-pass filter at the controller input and output, one obtains the results shown in Fig. 5b. The actuator signal seen by the Sierra sensor is smooth. The high-frequency components in the pressure sensor signal are essentially suppressed. The controller input is noise free, but a phase is introduced by the filter.

In practical applications, quantization errors resulting from the A/D conversion could alter the controller performance. This issue is generally examined by representing the quantized signal as the sum of an unquantized signal plus a noise term. This aspect is not addressed here because our main objective is to establish a methodology for active control simulations.

## Active Control Simulation Results

An instability control algorithm, noise source control (NSC), described by Mettenleiter et al.,[24] is used in the simulations presented in this section. It is based on an LMS method. To control the C1 flow, it is first necessary to identify the system seen by the controller. This is designated as the secondary path, which combines the chamber dynamics and the AAF and low-pass filter (LPF) transfer functions. (The model does not capture the flow dynamics separately.) With this information, the controller filter may be brought to convergence to a steady solution.

### Secondary Path Identification

Offline identification is used in the context of this simulation to describe the secondary path. As in experiments, it is possible to get this information in two regimes of operation:

1) Identification may be carried out in the presence of the vortex instability phenomenon.

2) Identification may be carried out in the absence of vortex shedding. This is achieved by multiplying the viscosity by a factor that is typically of the order of 20.

During identification, the controller RAC delivers a frequency that varies linearly in time (a siren signal). The signal detected by the pressure sensor $p_A$ is recorded by RAC, and MATLAB® is used to calculate an infinite impulse response filter comprising 21 coefficients in its numerator and denominator.

Figure 6 displays the results obtained in the two cases. In Fig. 6a, the secondary path is estimated in the presence of vortex shedding. The peak at 2600 Hz corresponds to the self-excited instability. The pronounced valley around 2800 Hz could be the result of the nonlinear behavior of the system, which maintains its resonant behavior even when driven at a slightly different frequency. In Fig. 6b, the vortices are suppressed. In this second case, the peak in amplitude corresponding to the instability amplitude is reduced to a great extent, and this is also true for a second peak around 1800 Hz. The phase also changes notably as the viscosity coefficient is augmented. The filters reproduce the real behavior quite well. On physical grounds it seems more appropriate to use the identification result obtained in the presence of the vortex shedding process. The corresponding secondary path transfer function is used in what follows.

### Adaptive Control

The control loop is closed when the flow simulation has reached a limit cycle with a well-established vortex shedding instability. Figure 7 shows the time evolution using different sensors after the controller is switched on. This event is represented by a vertical line. The error signal (pressure sensor $p_A$) is shown at the top of Fig. 7a. A considerable reduction is observed in the beginning, but the algorithm does not converge to a steady state. A stationary solution is reached after a transient phase featuring short modulations. The actuator signal shown at the bottom of Fig. 7a also features pulsations before converging to a steady state. Notice that a large amplitude is

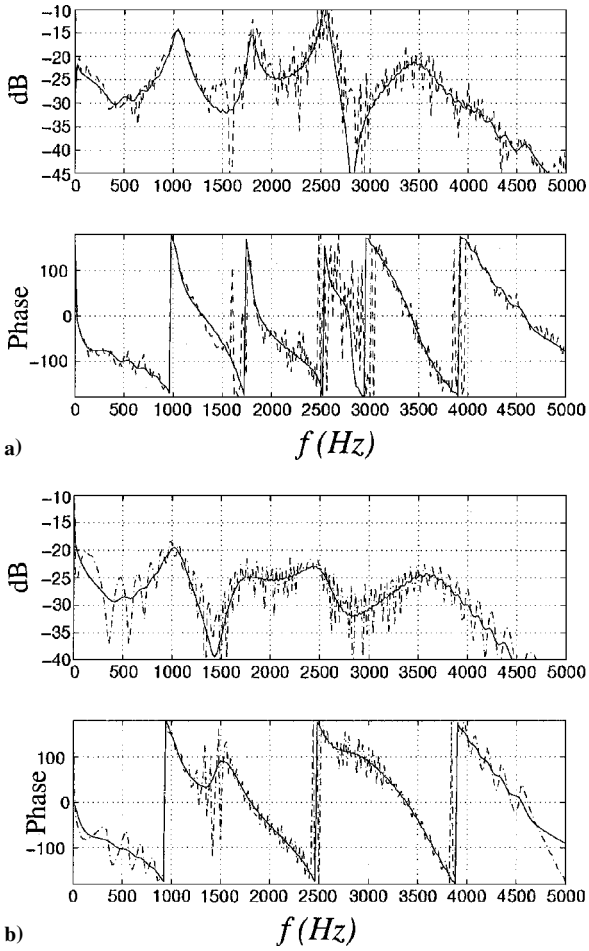


**Fig. 6 Real (-·-) and estimated (——) secondary path IIR filter: identification carried out a) in the presence of vortex shedding and b) with an augmented viscosity coefficient.**

initially generated to act on the process. This amplitude diminishes later and converges to a lower level when the signal becomes stationnary. To check the stability of the controlled state, many cycles were calculated after the stabilized amplitude was reached. Except for a slight increase in controller output, a stable behavior is observed. This behavior is also noticed in experiments,[24] suggesting that the controller acts on the vortex shedding process that drives the oscillation in the system.

This interpretation is confirmed by the velocity signal $u_E$ shown at the bottom of Fig. 7b. After an initial phase with modulations, the amplitude is stabilized at a lower level. The frequency also changes and the shift during the transition may be the source of modulations detected by all of the sensors. Finally, the pressure sensor $p_H$ placed on the motor front end (displayed at the top of Fig. 7b) features a notable reduction of amplitude when the controller is on, although it is worth recalling that this signal is not used in the control process.

The power spectral densities calculated during steady-state operation confirm the controller influence on the instability phenomenon. Figure 8a shows the spectral density of the pressure signal $p_A$ without and with control. The component at the instability frequency vanishes completely (>40 dB), but a new peak appears at a different frequency at a much reduced level (factor of 10). The spectral density of the velocity signal $u_E$ can be seen in Fig. 8b. It clearly shows that the oscillation is shifted to a higher frequency. The initial peak has disappeared. The new component reaches a significantly reduced level (factor of 3). This peak at 3900 Hz is close to the 3L mode of the C1 configuration, which corresponds to the next available mode for acoustic resonance. (This explains the small peak appearing in Fig. 8.) A similar behavior can be observed for the pressure signal $p_H$. The peak at the initial frequency vanishes, and the phenomenon is shifted to the higher mode. The overall level is reduced by a factor of 3. These results are not shown here.

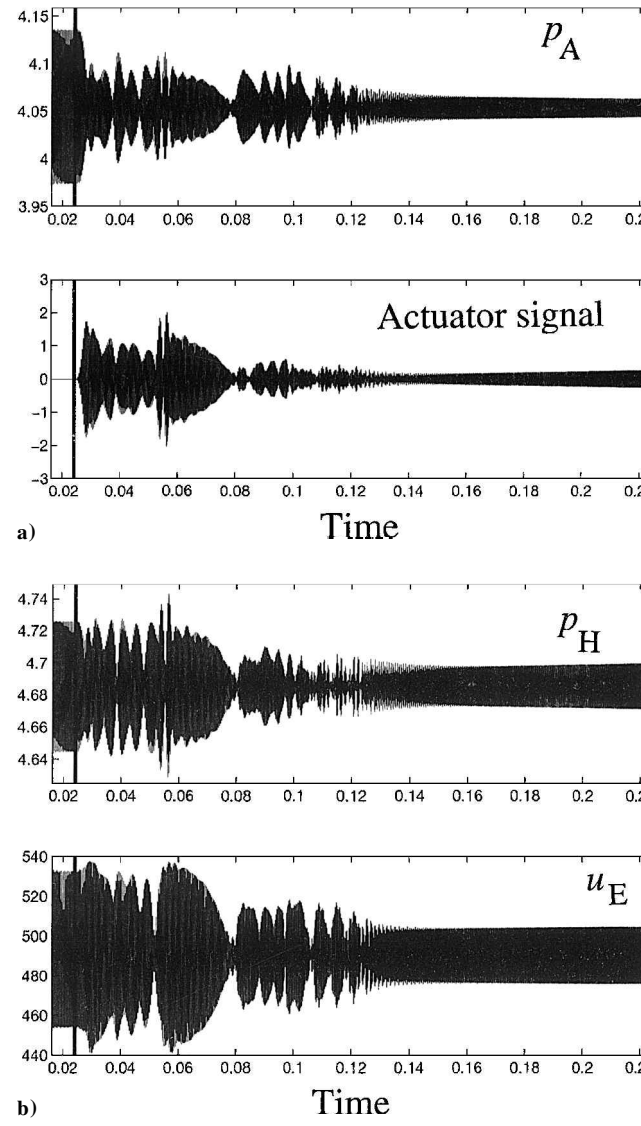


**Fig. 7 Control results in case 1. Signal records before and after the controller is switched on (vertical line indicates control switch on): a) top, error sensor $p_A$ and bottom, actuator signal; and b) top, pressure sensor $p_H$ and bottom, velocity signal $u_E$.**

The controller does not suppress the vortex shedding, but it shifts the phenomenon to another eigenmode. The intensities at this new frequency are nevertheless significantly reduced. The vorticity field before and after control is displayed in Fig. 9. The no-slip condition imposed at the head end produces a vorticity layer in the first columns of computational cells, but this has no consequence for the calculation. Figure 9b corresponding to the controlled operation shows that coherent vortices are still present, but their size and shedding frequency are modified in agreement with observations of the velocity spectral density.

It appears that in the numerical simulation the vortex shedding is more persistent than in the experimental case. This could be explained by the difference in the broadband content of the signals detected in the two situations. Without coupling, the acoustic signal is submerged in the broadband noise existing in the experimental facility, and it cannot trigger the vortices in a coherent fashion. The shedding takes place more randomly (demonstrated in experiments described by Mettenleiter[23]), or it may even be completely suppressed as described by Huang and Weaver.[25] In the numerical simulation, the flow conditions are much cleaner. There is no broadband noise, which could prevent the synchronization between acoustics and vortex dynamics. The vortices find, in all circumstances, a phase reference, even when the acoustic signal level is strongly reduced. No attempt was made to introduce broadband noise to simulate more realistic conditions.

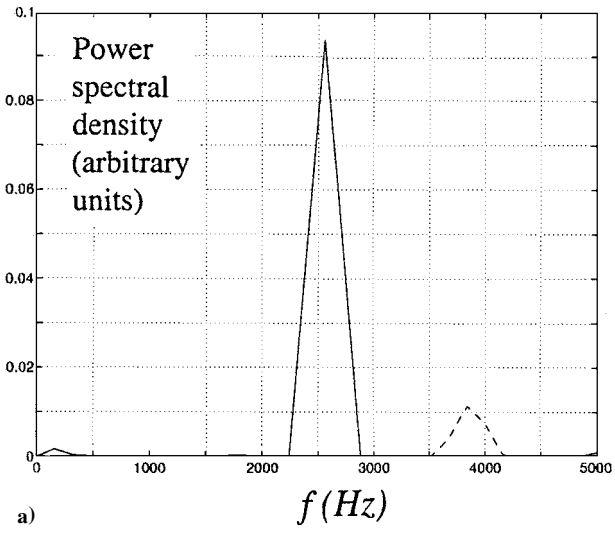


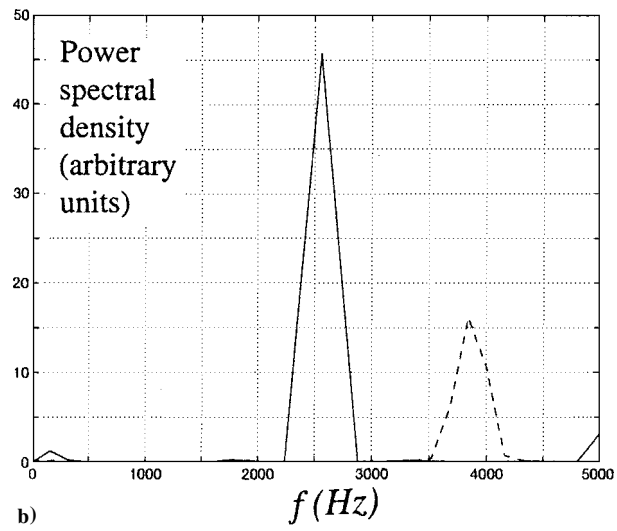


Fig. 8 Power spectral densities without (——) and with (– – –) control: power spectral density of a) pressure $p_A$ and b) velocity $u_E$.

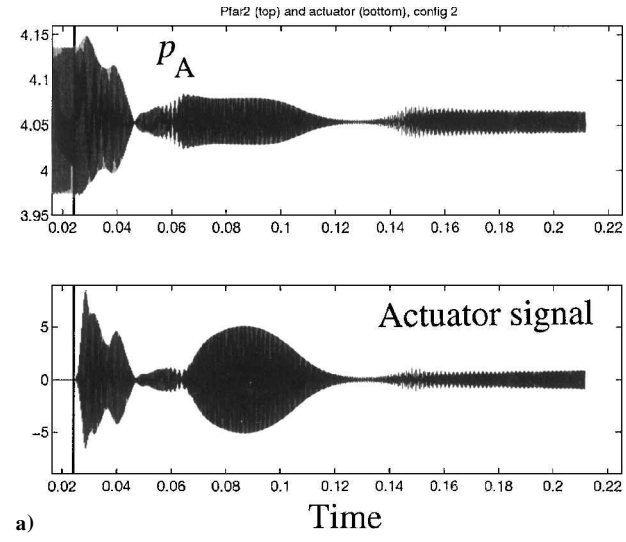


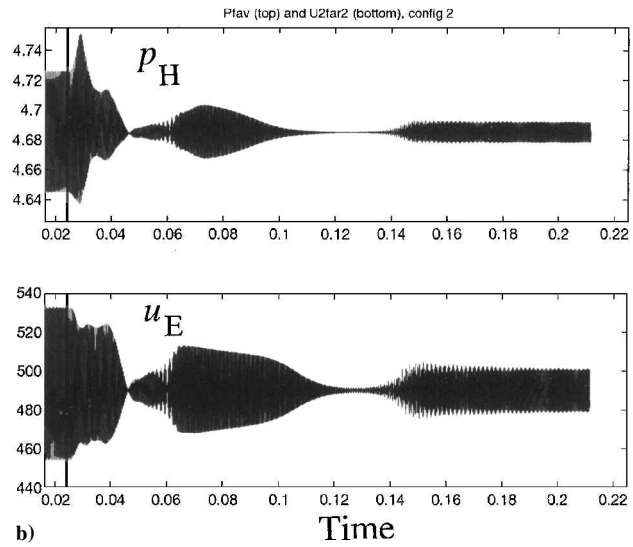


Fig. 10 Control results obtained in case 2; vorticity sensor $\omega_E$ provides the input to the controller; a) top, pressure sensor $p_A$, bottom actuator signal, and b) top pressure sensor $p_H$, and bottom velocity signal $u_E$. Vertical line indicates control switch on.

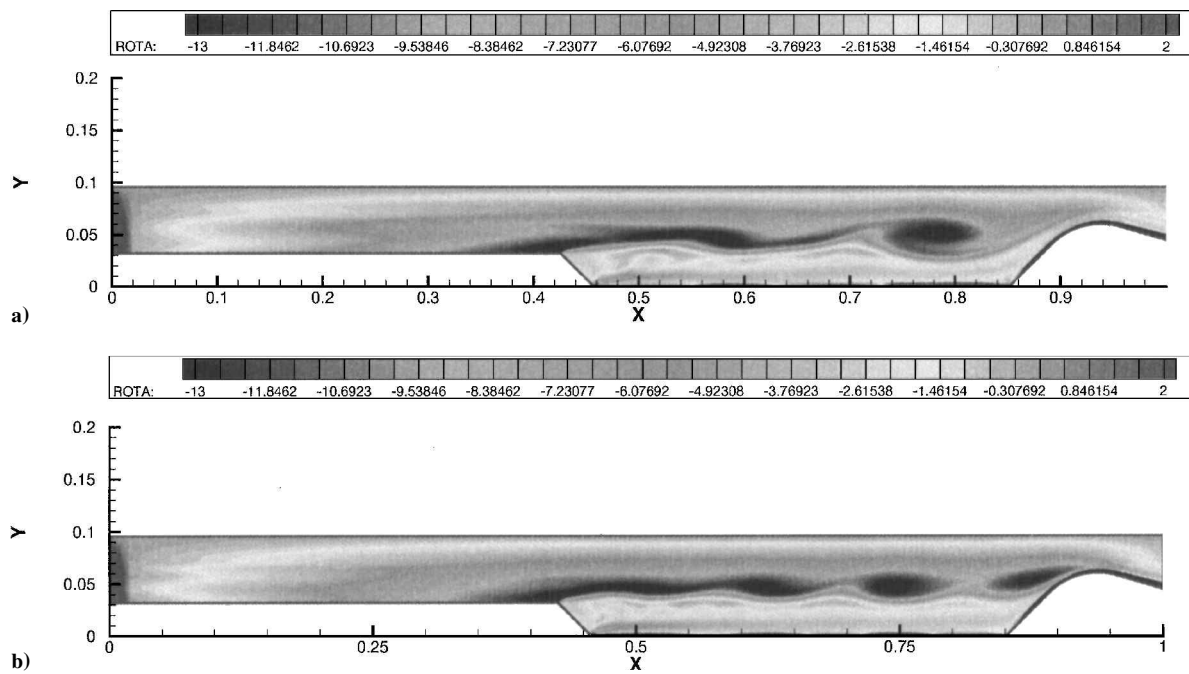


Fig. 9 Controller input is the pressure signal $p_A$ (case 1): vorticity field a) before and b) after control.

In the case examined, the controller acts on the acoustics and then indirectly through coupling on the vortex shedding. A more efficient reduction of velocity fluctuations could be obtained by acting directly on the shear layer. It is interesting to see whether an additional decrease in the signal amplitude could be obtained with a new arrangement in which the actuator is set at the edge of the propellant surface and the sensor provides a vorticity signal (case 2 in Table 1). After identification of the secondary path corresponding to this new setup (with vortex shedding), a new simulation is carried out. Figure 10 shows the pressure signal $p_A$ (Fig. 10a, top) and $p_H$ (Fig. 10b, top). The actuator signal is at the bottom of Fig. 10a. The velocity sensor $u_E$ appears at the bottom of Fig. 10b. Reduction of this last signal is effectively more direct than in the preceding calculation (compare Figs. 7 and 10). The pressure sensors also behave in a different manner. The pressure levels are first slightly augmented, reduction taking place in a second stage (Fig. 10). The same increase is observed in the velocity fluctuation for the first simulation (Fig. 7).

The reduction in amplitude obtained in the steady state may be compared to that obtained earlier. In general, the same frequency shift can be observed as in case 1. The initial peaks disappear, and the oscillation is shifted to the 3L mode, with a largely reduced level. Spectral densities of the different signals are shown in Fig. 11. The pressure signal $p_A$ is slightly lower in case 1 than in case 2. This is not surprising because this signal is to be minimized in the first arrangement. In case 2, the pressure level at the front end is lower, and the velocity fluctuations $u_E$ are diminished by a factor of 4.5. The overall reduction in the error sensor (a vorticity signal) is also considerable. As for the other sensors, the initial frequency has disappeared, and the 3L peak appears with a level reduced by a factor of 6.3. (This result is not shown here.) Also note that convergence in the second case is smoother, perhaps because the controller acts more directly on the instability process. Note that between $t = 0.12$ and $t = 0.14$ s, all signals are reduced significantly (Fig. 10). This reduction is, unfortunately, not maintained, and the signals reach a steady state at a greater level. There are some possible reasons for this behavior. The frequency shift drives the controller toward a new solution. As the sensor level is greatly reduced, the rate of convergence for this new situation is diminished. (A factor of 10 reduction in amplitude reduces the convergence rate by a factor of 100.) One may also invoke the fact that the sensor signal is too clean. In the numerical calculation, the error signal $e$ detected by the sensor cannot be driven to zero because this would not lead to a steady state of the controller (see Ref. 23 or 24 for more details). The controller action would tend to zero, but with a vanishing output the instability mechanism would not be controllable. This scenario requires further testing.

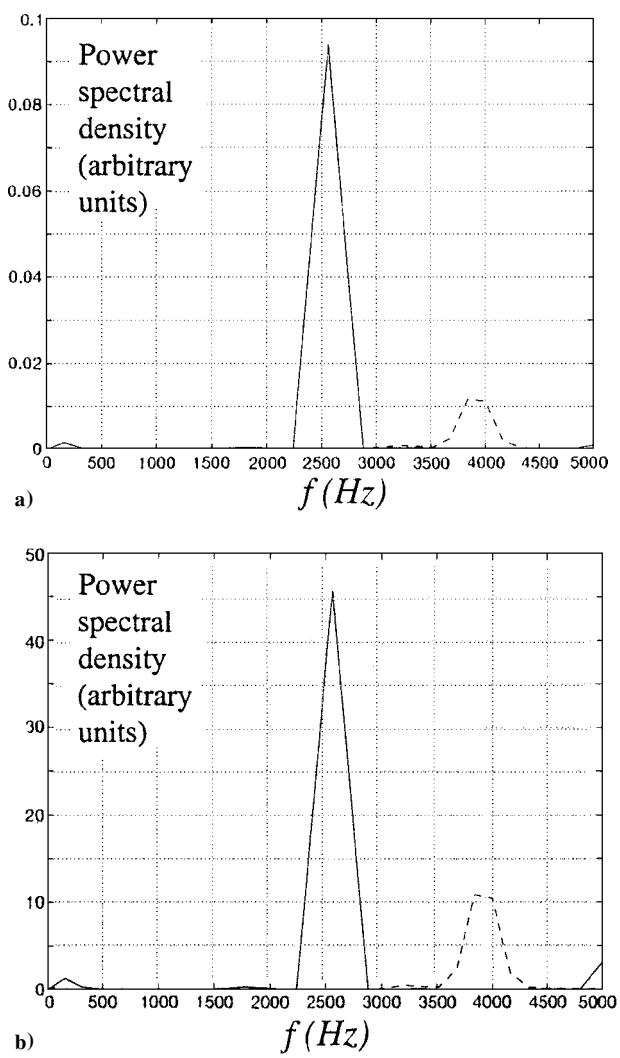


**Fig. 11 Power spectral densities without (——) and with (– – –) control: a vorticity sensor provides the input to the controller (case 2): spectral density of a) pressure $p_A$ and b) velocity $u_E$.**

**Fig. 12 Vorticity field at $t = 0.1264$ s: control achieved with a vorticity sensor $\omega_E$ and an actuator located at the propellant surface edge (case 2).**

Figure 12 shows the vorticity distribution at a point in time ($t = 0.1264$ s) where the level of fluctuations is quite small. Coherent vortices have essentially disappeared from the flowfield, and the shear layer develops without rollup.

## Conclusions

The simulation of active control is investigated. A Navier–Stokes solver is coupled to an adaptive control algorithm. It is shown that the actuator may be defined by distributing sources in the computational domain. This method is first used in open-loop tests. The coupling of the flow simulation module with the control algorithm is then considered. Because the rates of operation of the flow solver and active control are widely different, the signals at the controller input and output must be filtered. It is shown that this eliminates high-frequency components that would otherwise perturb the calculation. The simulation of active control is then developed in a solid rocket motor geometry in which vortex shedding takes place, which leads to acoustic resonance of the system. Results obtained demonstrate that control is feasible and that the method may be used to examine the changes in the flowfield induced by the controller. However, convergence and stability issues related to adaptive control algorithms would need further investigation.

## Acknowledgments

This work is part of the Aerodynamics of Segmented Solid Motors research program coordinated by the Centre National d'Etudes Spatiales (CNES) and ONERA. The support of CNES is gratefully acknowledged.

## References

[1]Blomshield, F., and Mathes, H. B., "Pressure Oscillations in Post-Challenger Space Shuttle Redesigned Solid Rocket Motors," *Journal of Propulsion and Power*, Vol. 9, No. 2, 1993, pp. 217–221.

[2]Vuillot, F., "Vortex Shedding in Solid Rocket Motors," *Journal of Propulsion and Power*, Vol. 11, No. 4, 1995, pp. 626–639.

[3]Dotson, K. W., Koshigoe, S., and Pace, K. K., "Vortex Shedding in a Large Solid Rocket Motor Without Inhibitors at the Segment Interfaces," *Journal of Propulsion and Power*, Vol. 13, No. 2, 1997, pp. 197–206.

[4]Le Breton, P., Guéry, J.-F., Vuillot, F., and Prevost, M., "Recent Advances in the Prediction of SRM Thrust Oscillations," *Proceedings of the 1st European Colloquium on Launcher Technology*, Centre National d'Etudes Spatiales, Toulouse, France, 1999.

[5]Lupoglazoff, N., and Vuillot, F., "Two-Dimensional Numerical Simulation of the Stability of Solid Propellant Solid Rocket Motor," AIAA Paper 91-0205, Jan. 1991.

[6]Koshigoe, S., Gillis, J. T., and Falangas, E. T., "A New Approach for Active Control of Sound Transmission Through an Elastic Plate Backed by

a Rectangular Cavity," *Journal of the Acoustical Society of America*, Vol. 97, No. 2, 1993, pp. 900–907.

[7]Koshigoe, S., Teagle, A., and Gordon, A., "A Time Domain Study of Active Control of Sound Transmission due to Acoustic Pulse Excitation," *Journal of the Acoustical Society of America*, Vol. 97, No. 1, 1995, pp. 313–323.

[8]Koshigoe, S., Teagle, A., Tsay, C.-H., Morishita, S., and Une, S., "Numerical Simulation of Active Control with On-Line System Identification of Sound Transmission Through an Elastic Plate," *Journal of the Acoustical Society of America*, Vol. 99, No. 5, 1996, pp. 2947–2954.

[9]Koshigoe, S., Teagle, A., and Tsay, C.-H., "A Rapidly Convergent Adaptive Controller Applied to Suppression of Random Noise Transmission," *Journal of Vibration and Acoustics*, Vol. 120, 1998, pp. 449–454.

[10]Hathout, J. P., Annaswamy, A. M., Fleifil, M., and Ghoniem, A. F., "A Model-Based Active Control Design for Thermoacoustic Instability," *Combustion Science and Technology*, Vol. 132, 1998, pp. 99–138.

[11]Annaswamy, A. M., El Rifai, O. M., Fleifil, M., Hathout, J. P., and Ghoniem, A. F., "A Model-Based Self-Tuning Controller for Thermoacoustic Instability," *Combustion Science and Technology*, Vol. 135, 1998, pp. 213–240.

[12]Culick, F. E. C., Lin, W. H., Jahnke, C. C., and Sterling, J. D., "Modeling for Active Control of Combustion and Thermally Driven Oscillations," *Proceedings of the American Control Conference*, Inst. of Electrical and Electronics Engineers, Piscataway, NJ, 1991.

[13]Yang, V., and Fung, Y. T., "Active Control of Nonlinear Pressure Oscillations in Combustion Chambers," *Journal of Propulsion and Power*, Vol. 8, No. 6, 1992, pp. 1282–1289.

[14]Annaswamy, A. M., Fleifil, M., Hathout, J. P., and Ghoniem, A. F., "Impact of Linear Coupling on the Design of Active Controllers for the Thermoacoustic Instability," *Combustion Science and Technology*, Vol. 128, 1997, pp. 131–180.

[15]Koshigoe, S., Komatsuzaki, T., and Yang, V., "Adaptive Control of Combustion Instability with OnLine System Identification," *Journal of Propulsion and Power*, Vol. 15, No. 3, 1999, pp. 383–389.

[16]Menon, S., "Active Combustion Control in a Ramjet Using Large-Eddy Simulations," *Combustion Science and Technology*, Vol. 84, 1992, pp. 51–79.

[17]Neumeier, Y., and Zinn, B., "Active Control of Combustion Instabilities Using Real Time Identification of Unstable Combustor Modes," *Proceedings of the IEEE Conference on Control Applications*, IEEE Publications, Piscataway, NJ, 1995, pp. 691–698.

[18]Kestens, T., "Etude Numérique du Contrôle Adaptatif Multivoies des Instabilités Aéroacoustiques des Cavités," Ph.D. Dissertation, Institut National Polytechnique de Toulouse, Toulouse, France, 1999.

[19]Jameson, A., and Schmidt, W., "Some Recent Developments in Numerical Methods for Transonic Flows," *Computer Methods in Applied Mechanics and Engineering*, Vol. 51, 1985, pp. 467–493.

[20]Lupoglazoff, N., and Vuillot, F., "Numerical Simulations of Vortex Shedding Phenomenon in Two-Dimensional Test Case Solid Rocket Motors," AIAA Paper 92-0776, Jan. 1992.

[21]Comte, P., Silvestrini, J. H., and Begou, P., "Streamwise Vortices in Large-Eddy Simulations of Mixing Layers," *European Journal of Mechanics B*, Vol. 17, 1998, pp. 615–637.

[22]Mohanraj, R., Neumeier, Y., and Zinn, B. T., "Characteristic-Based Treatment of Source Terms in Euler Equations for Roe Scheme," *AIAA Journal*, Vol. 37, No. 4, 1999, pp. 417–424.

[23]Mettenleiter, M., "Contrôle Adaptatif des Instabilités Aéroacoustiques," Ph.D. Dissertation, Ecole Centrale Paris, Châtenay-Malabry, France, Feb. 2000.

[24]Mettenleiter, M., Haile, E., and Candel, S., "Adaptive Control of Aeroacoustic Instabilities," *Journal of Sound and Vibration*, Vol. 230, No. 4, 2000, pp. 761–789.

[25]Huang, X. Y., and Weaver, D. S., "On the Active Control of Shear Layer Oscillations Across a Cavity in the Presence of Pipeline Acoustic Resonance," *Journal of Fluids and Structures*, Vol. 5, 1991, pp. 207–219.

P. Givi
*Associate Editor*